Journal of Low Temperature Physics manuscript No.
(will be inserted by the editor)

Fabrication of detector arrays for the SPT-3G receiver

C. M. Posada[a] · **P. A. R. Ade**[b] · **Z. Ahmed**[c,d,e] · **A. J. Anderson**[f,g] · **J. E. Austermann**[h] · **J. S. Avva**[i] · **R. Basu Thakur**[g] · **A. N. Bender**[j,g] · **B. A. Benson**[f,g,k] · **J. E. Carlstrom**[g,l,m,j,k] · **F. W. Carter**[j,g] · **T. Cecil**[j] · **C. L. Chang**[j,g,k] · **J. F. Cliche**[n] · **A. Cukierman**[i] · **E. V. Denison**[h] · **T. de Haan**[i] · **J. Ding**[a] · **R. Divan**[o] · **M. A. Dobbs**[n,p] · **D. Dutcher**[g,m] · **W. Everett**[q] · **A. Foster**[r] · **R. N. Gannon**[a] · **A. Gilbert**[n] · **J. C. Groh**[i] · **N. W. Halverson**[q,s] · **A. H. Harke-Hosemann**[t,j] · **N. L. Harrington**[i] · **J. W. Henning**[g] · **G. C. Hilton**[h] · **W. L. Holzapfel**[i] · **N. Huang**[i] · **K. D. Irwin**[c,d,e] · **O. B. Jeong**[i] · **M. Jonas**[f] · **T. Khaire**[a] · **A. M. Kofman**[u,t] · **M. Korman**[r] · **D. Kubik**[f] · **S. Kuhlmann**[j] · **C. L. Kuo**[c,d,e] · **A. T. Lee**[i,v] · **A. E. Lowitz**[g] · **S. S. Meyer**[g,l,m,k] · **D. Michalik**[k] · **C. S. Miller**[o] · **J. Montgomery**[n] · **A. Nadolski**[t] · **T. Natoli**[w] · **H. Nguyen**[f] · **G. I. Noble**[n] · **V. Novosad**[a] · **S. Padin**[g] · **Z. Pan**[g,m] · **J. Pearson**[a] · **A. Rahlin**[f,g] · **J. E. Ruhl**[r] · **L. J. Saunders**[j,g] · **J. T. Sayre**[q] · **I. Shirley**[i] · **E. Shirokoff**[g,k] · **G. Smecher**[x] · **J. A. Sobrin**[g,m] · **L. Stan**[o] · **A. A. Stark**[y] · **K. T. Story**[c,d] · **A. Suzuki**[i,v] · **Q. Y. Tang**[g,k] · **K. L. Thompson**[c,d,e] · **C. Tucker**[b] · **L. R. Vale**[h] · **K. Vanderlinde**[w,z] · **J. D. Vieira**[t,u] · **G. Wang**[j] · **N. Whitehorn**[aa,i] · **V. Yefremenko**[j] · **K. W. Yoon**[c,d,e] · **M. R. Young**[z]

the date of receipt and acceptance should be inserted later

[a]Argonne National Laboratory, Material Science Division, 9700 S. Cass Ave., Argonne, IL 60439 · [b]School of Physics and Astronomy, Cardiff Univ., Cardiff CF24 3YB, United Kingdom · [c]Kavli Institute for Particle Astrophysics and Cosmology, Stanford Univ., 452 Lomita Mall, Stanford, CA 94305 · [d]Dept. of Physics, Stanford Univ., 382 Via Pueblo Mall, Stanford, CA 94305 · [e]SLAC National Accelerator Laboratory, 2575 Sand Hill Rd., Menlo Park, CA 94025 · [f]Fermi National Accelerator Laboratory, MS209, P.O. Box 500, Batavia, IL 60510-0500 · [g]Kavli Institute for Cosmological Physics, Univ. of Chicago, 5640 S. Ellis Ave., Chicago, IL 60637 · [h]National Institute of Standards and Technology, 325 Broadway, Boulder, CO 80305 · [i]Dept. of Physics, Univ. of California, Berkeley, CA 94720 · [j]Argonne National Laboratory, High-Energy Physics Division, 9700 S. Cass Ave., Argonne, IL 60439 · [k]Dept. of Astronomy and Astrophysics, Univ. of Chicago, 5640 S. Ellis Ave., Chicago, IL 60637 · [l]Enrico Fermi Institute, Univ. of Chicago, 5640 S. Ellis Ave., Chicago, IL 60637 · [m]Dept. of Physics, Univ. of Chicago, 5640 S. Ellis Ave., Chicago, IL 60637 · [n]Dept. of Physics, McGill Univ., 3600 Rue University, Montreal, Quebec H3A 2T8, Canada · [o]Argonne National Laboratory, Center for Nanoscale Materials, 9700 S. Cass Ave., Argonne, IL 60439 · [p]Canadian Institute for Advanced Research, CIFAR Program in Cosmology and Gravity, Toronto, ON, M5G 1Z8, Canada · [q]CASA, Dept. of Astrophysical and Planetary Sciences, Univ. of Colorado, Boulder, CO 80309 · [r]Physics Dept., Case Western Reserve Univ., Cleveland, OH 44106 · [s]Dept. of Physics, Univ. of Colorado, Boulder, CO 80309 · [t]Astronomy Dept., Univ. of Illinois, 1002 W. Green St., Urbana, IL 61801 · [u]Dept. of Physics, Univ. of Illinois, 1110 W. Green St., Urbana, IL 61801 · [v]Physics Division, Lawrence Berkeley National Laboratory, Berkeley, CA 94720 · [w]Dunlap Institute for Astronomy and Astrophysics, Univ. of Toronto, 50 St George St, Toronto, ON, M5S 3H4, Canada · [x]Three-Speed Logic, Inc., Vancouver, B.C., V6A 2J8, Canada · [y]Harvard-Smithsonian Center for Astrophysics, 60 Garden St., Cambridge, MA 02138 · [z]Dept. of Astronomy and Astrophysics, Univ. of Toronto, 50 St George St, Toronto, ON, M5S 3H4, Canada · [aa]Dept. of Physics and Astronomy, Univ. of California, Los Angeles, CA 90095

Abstract The South Pole Telescope third-generation (SPT-3G) receiver was installed during the austral summer of 2016-17. It is designed to measure the cosmic microwave background across three frequency bands centered at 95 GHz, 150 GHz and 220 GHz. The SPT-3G receiver has ten focal plane modules, each with 269 pixels. Each pixel features a broad-band sinuous antenna coupled to a niobium microstrip transmission line. In-line filters define the desired band-passes before the signal is coupled to six bolometers with Ti/Au/Ti/Au transition edge sensors (3 bands x 2 polarizations). In total, the SPT-3G receiver is composed of 16,000 detectors, which are readout using a 68x frequency domain multiplexing scheme. In this paper, we present the process employed in fabricating the detector arrays.

Keywords Bolometers, Cosmic Microwave Background, TES detectors, Multichroic Sensors, SPT-3G

1 Introduction

The cosmic microwave background (CMB) is remnant radiation from the early universe, providing a unique window for exploring fundamental physics [1]. Precise measurements of the CMB have the potential to detect primordial gravitational waves generated during inflation, constrain the number of relativistic particles, as well as the sum of neutrino masses, and characterize dark energy and dark matter[2]. Current and upcoming CMB experiments focus on characterizing the B-mode polarization, which requires receivers with exquisite sensitivity [3]. Current CMB detectors are background limited, so higher sensitivity requires more detectors.

SPT-3G is the third generation receiver for measurements of the CMB with the South Pole Telescope[4]. It has an order of magnitude more detectors than previous experiments[5]. In the following sections, we describe the fabrication process for the SPT-3G detectors.

2 SPT-3G Focal Plane and Detector Architecture

The SPT-3G focal plane is comprised of ten hexagonal arrays of detectors fabricated on 150 mm Si wafers. Each array of detectors is composed of 269 antenna-coupled multichroic pixels plus two pixels containing the alignment marks required for stepper lithography. In total, each pixel has six transition edge sensors (TES) [6], sensitive to three frequency bands and two linear polarizations, for 16,000 detectors in the focal plane. We use a 68x frequency multiplexing (DfMUX) scheme to read out the detectors [7, 8]. Fig. 1 *(Top-Left)* shows one of the finished SPT-3G detector arrays. Fig. 1 *(Right)* shows the pixel details. Each pixel has a broad-band, polarization-sensitive sinuous antenna coupled to a Nb microstrip transmission line [9, 10]. In-line three-pole filters split the CMB signal into three frequency bands centered at 95 GHz, 150 GHz and 220 GHz [11, 12]. Once the passbands are defined, the signal is terminated and thermalized using a 20 Ohm Ti/Au load resistor. The resistor and TES are located on the bolometer island, a membrane suspended by four long, narrow legs, Fig. 1 *(Middle-left)*. The change in temperature of the island is sensed by a Ti/Au/Ti/Au TES biased in its transition. An 850 nm layer of Pd is deposited on the island to increase the heat capacity, so the bolometers are stable when operated with constant voltage bias for strong electrothermal feedback [6]. As seen in Fig. 1 *(Bottom-left)* Si under the bolometer island and legs is removed to thermally isolate the island from the substrate. The four long, narrow legs define the detectors' weak thermal link to the substrate (heat bath) [13, 14].

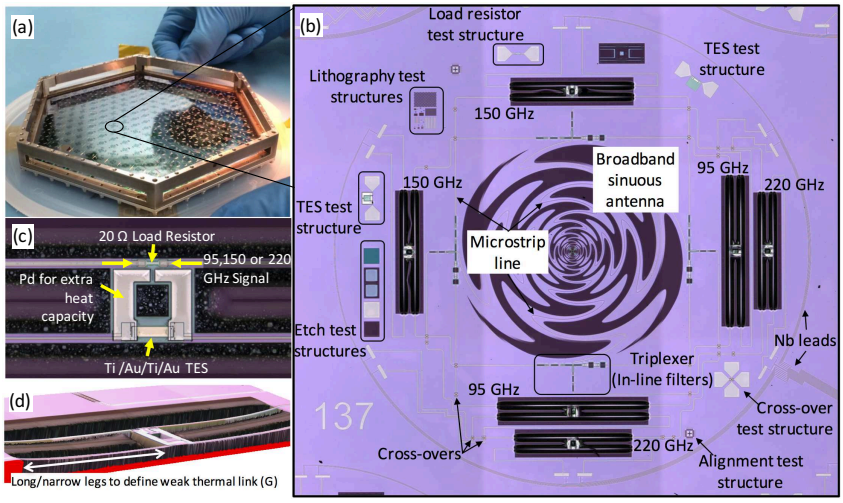

Fig. 1 *(Top-left)* One of the SPT-3G detector arrays mounted in its invar holder. *(Right)* Overview of a SPT-3G multichroic pixel showing a sinuous antenna coupled through a Nb microstrip transmission line to six Ti/Au/Ti/Au TES bolometers. *(Middle-left)* Top view of a bolometer island, showing the Ti/Au load resistor, Ti/Au/Ti/Au TES and the Pd layer deposited for extra heat capacity. *(Bottom-Left)* Isometric view of one SPT-3G bolometer. The bolometer island is suspended by four long, narrow legs that define the weak thermal link (G) between the island and the substrate. For a given TES T_c, the geometry of the legs determines the detector's saturation power for each of the three passbands. (Color figure online.)

3 Fabrication Process

The fabrication of each detector wafer involved 15 lithography steps, 8 RIE-ICP etching processes and 9 depositions, including 7 metallic and 2 dielectric layers. We used stepper lithography for all steps, except for the array-level wiring, which was patterned using optical contact lithography. We carried out the fabrication of these wafers at the Materials Science Division and the Center for Nanoscale Materials (CNM) at Argonne National Laboratory. These wafers were processed in batches of five and each batch took an average of 21 days to be completed. The detectors fabrication process flow is presented in Fig 2. Previous reports on the development, stabilization and optimization of the fabrication process as well as details that are outside the scope of this paper are presented elsewhere [15, 16].

We start the fabrication process by etching the alignment marks used for stepper lithography. This step is followed by the deposition and patterning of the Nb ground plane and deposition of the SiO_x that serves as dielectric in our microstrip[17]. The sinuous antenna, size and geometry of the bolometers, and the initial components of the in-line filters are defined in the Nb ground plane. The target thickness of the SiO_x dielectric layer is 500 nm. The thickness of this layer defines the passband centers of our detectors[18]. We controlled the thickness of this dielectric layer to within 3% of its target value to prevent the passbands from overlapping with atmospheric emission lines.

The 20 Ohm Ti/Au (50 nm / 7 nm) load resistor is deposited on the SiO_x layer. This is followed by the lift-off of our Ti/Au/Ti/Au TES. The relative thicknesses of the Ti and Au layers in the TES define its superconducting transition temperature (T_c) and normal resistance (R_n) [19]. To accommodate uncertainties in optical loading at the South Pole, we fabricated detector arrays with a range of T_c between 500 mK and 550 mK for the

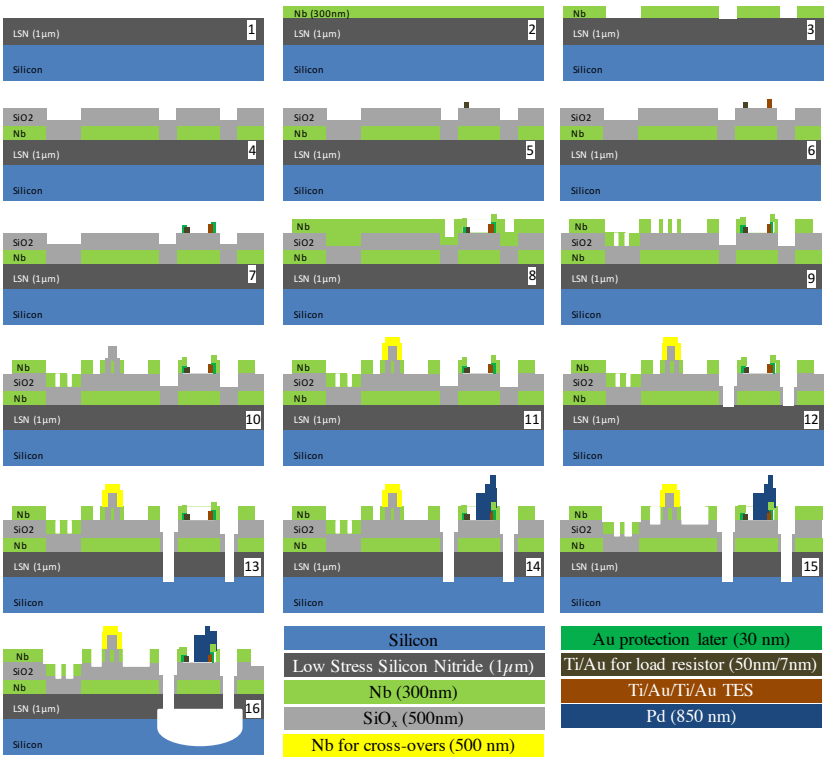

Fig. 2 Step-by-step fabrication process of the arrays of detectors deployed with the SPT-3G receiver. *(1)* ICP-RIE etching of 140 nm deep alignment marks in the LSN layer for stepper lithography. *(2)* DC Magnetron Sputtering of 300 nm of Nb (Nb ground) *(3)* Nb ground plane ICP-RIE etching using a CHF_3/SF_6 based plasma chemistry. *(4)* Deposition of a 500 nm layer of SiO_x by DC magnetron reactive sputtering. *(5)* Lift-off of a Ti/Au (50 nm/7 nm) layer to define the 20 Ohm load resistor. *(6)* Lift-off of the Ti/Au/Ti/Au quadlayer TES. Target T_c=450 mK, target and R_n=2.0 Ohms. *(7)*Deposition of a thin Ti/Au bilayer (5 nm/30 nm) on the edges of the resistors and TESs. Deposition and patterning of the 300 nm Nb top layer is carried out using a two step process: *(8)* Lift-off of the 300 nm Nb top layer. *(9)* ICP-RIE etching of the Nb using an SF_6/CHF_3 plasma chemistry. *(10)* Deposition and lift-off of a 400 nm SiO_2 layer used as spacer in the three layer $Nb/SiO_2/Nb$ cross-over structures. *(11)* Lift-off of a 500 nm Nb layer used to complete the three layer cross-over structures. *(12)* SiO_x etching using an ICP-RIE process based on a CHF_3/Ar plasma chemistry. *(13)* Etching of trenches into the SIN_x layer to expose the Si around the legs of the bolometers. *(14)* Deposition of an 850 nm layer of Pd on the island to stabilize the detectors. *(15)* ICP-RIE etch process to clean Nb residuals. *(16)* Dicing of the arrays into their final hexagonal shape followed by a XeF_2 dry etching process to remove the Si from underneath the detectors and define their thermal weak link (G). The fabrication is completed by a final O_2 ashing step in which left-over photoresist is removed from the surface of the wafer. (Color figure online.)

2017 deployment. For this set of detectors, we measured R_n around 2.2 Omhs and P_{sat} between 15 pW and 30 pW. Further details on the thermal and electrical characterization of the deployed detectors, including details on the overall yield at cryogenic temperatures are presented elsewhere [20, 21].

We deposit a thin Ti/Au bilayer (5 nm / 30 nm) on the edges of the the resistors and TESs to prevent undesired interactions with the Nb top layer [22]. The Au in this layer acts

as a diffusion barrier between Nb and Ti, leading to sharp, smooth transitions with good long-term stability [16].

The Nb top layer is deposited and patterned using a two-step process. This allow us to connect to the TESs and resistors using a lift-off process, whereas the Nb microstrip and array-level wiring are defined using ICP-RIE etching. For the etching step of the Nb top layer, we define the Nb microstrip[17] within each pixel using stepper lithography, while we use optical contact lithography for the array-level wiring.

Once etching of the microstrip is completed, we fabricate three-layer Nb/SiO_2/Nb cross-over structures, where the films for the SiO_2 spacer and cross-over Nb are patterned by lift-off. In addition, we provide additional heat capacity to the island by depositing a 850 nm layer of Pd. The fabrication process is completed by etching trenches around the legs and islands of the bolometers to expose the Si substrate underneath. At this point, the wafers are diced into their final hexagonal shape. Finally, we carry out a XeF_2 chemical etching process to remove the Si from under the bolometers.

4 Improvements to the fabrication process

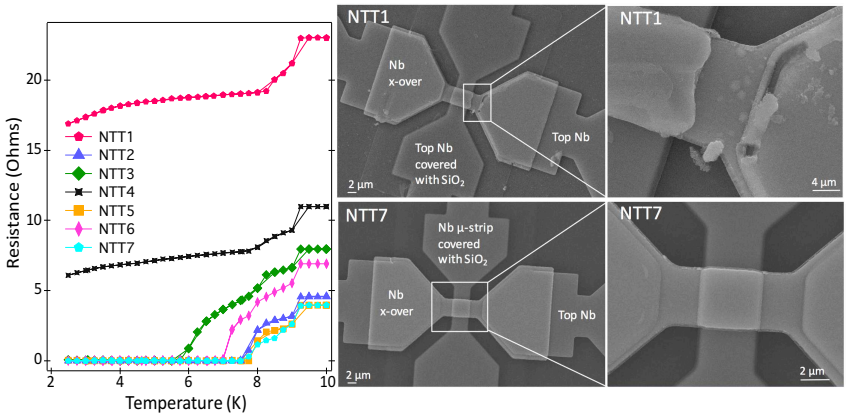

Fig. 3 *(Left)* $R(T)$ curves of Nb cross-over structures with the SiO_2 spacer patterned by lift-off using single and bilayer resist. Samples NTT1 to NTT4 were fabricated using single layer resist. Samples NTT5 to NTT7 were fabricated using bilayer resist. The process employed for sample NTT7 was incorporated into the fabrication of the cross-over structures in the full-array wafers. *(Right)* SEM image of cross-over samples. *(Top)* SEM of cross-overs fabricated using a single layer resist process for the SiO_2 lift-off. *(Bottom)* SEM of cross-overs fabricated using a bilayer resist process for the SiO_2 lift-off. (Color figure online.)

Feedback from laboratory testing of our detector wafers allowed us to change the fabrication process to improve the thermal and optical performance, as well as the uniformity of deployed detectors. The first of these improvements was the shift from a bilayer Ti/Au TES to a quadlayer Ti/Au/Ti/Au structure to isolate the TES from the substrate[19].

Another improvement was patterning of the cross-over SiO_2 by lift-off using a bilayer rather than a single layer resist. The SEM images of cross-over structures shown in Fig. 3 *(Top)* were fabricated using a single layer resist for the SiO_2 lift-off. This process led to high walls at the edges of the SiO_2 spacers, which caused damage to the Nb cross-over layer,

resulting in lower optical efficiency. Adopting a bilayer lift-off process reduced the height of the walls in the SiO_2 spacers, Fig. 4 *(Bottom)*.

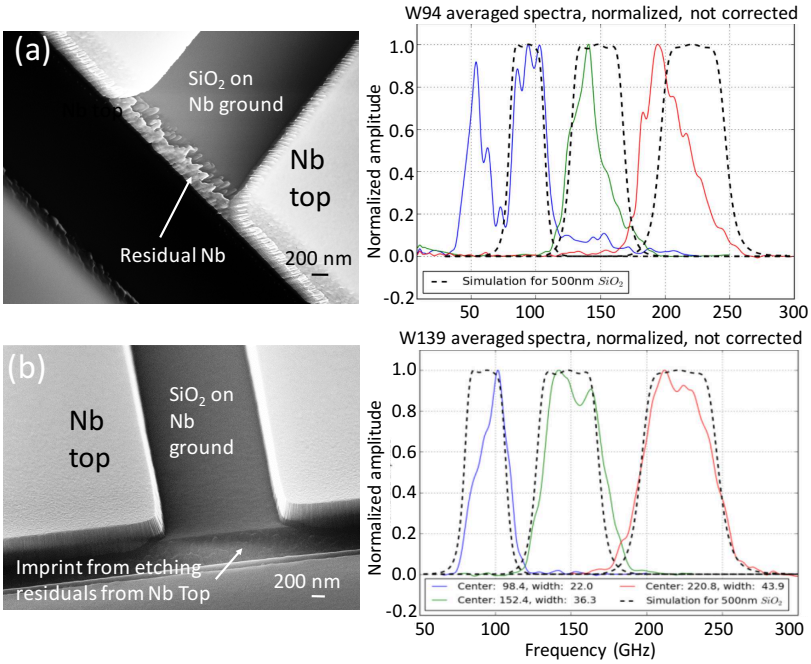

Fig. 4 *(Top-left)* SEM of the capacitor in one of the 95 GHz filters. It shows the Nb residue shorting this capacitor. *(Top-right)* Measured passbands of detectors known to have Nb residue in the steps in the filters and antenna. *(Bottom-left)* SEM of the capacitor in one of the 95 GHz filters after extra etch to remove Nb residual. *(Bottom-right)* Measured passbands of detectors where Nb residues were removed using an additional Nb etch process. (Color figure online.)

We also found the measured passbands of our detectors to be in disagreement with the designed bands, Fig. 4 *(Top-right)*. Using SEM imaging, we found these discrepancies to be caused by residual Nb left during etching of the Nb top layer, as shown in Fig. 4 *(Top-left)*. This residual Nb causes shorts in the capacitors. We solved the problem by including an additional ICP-RIE Nb etch to remove the residue where microstrip SiO_x covered steps in the Nb ground plane. In Fig. 4 *(Bottom-left)* we show SEM images of places where Nb residuals were originally present. The additional Nb etch gives repeatable bands that match the design, Fig. 4 *(Bottom-right)*. The top of the 95 GHz band shown Fig. 4 *(Bottom-right)* is not flat. This discrepancy with the simulation results indicates that the lower frequency components of this band are cut off by some of the optical elements in the cryostat. Additional details on the bands and the general optical characterization of the deployed detectors are presented elsewhere [18].

In addition, we found that defects induced by the use of contact lithography for patterning of the array-level wiring was limiting our maximum yield per wafer. We define yield for our detectors as the percentage of good TESs measured through room temperature continuity probing. As an alternative, we have replaced this step by a non-contact laser lithography step carried out using a Heidelberg MLA system. It has allowed us to go from a total yield

around 80-85% to 90-95%. For the 2017 observing season, the yield of operable bolometers at cryogenic temperatures was 75.8% [20]. Based on results obtained during the 2017 observing season [21], we have also fabricated a new set of detector wafers with updated target values for R_n=2.0 Ohms, T_c; 450mK and P_{sat} of 10.2 pW, 15.4 pW and 20.0 pW for the 95 GHZ, 150 GHz and 220 GHz detectors, respectively [20].

5 Conclusions

We fabricated and deployed a set of 10 detector wafers for the SPT-3G receiver, with 16,000 detectors. To improve the performance and yield, we included the following new features in the fabrication process: quadlayer Ti/Au/Ti/Au TES to isolate the TES from the substrate; better control of SiO_2 edges in cross-overs to minimize losses in the microstrip; additional local etching of Nb top to eliminate shorts due to Nb top residue on steps in Nb ground; laser writer patterning of Nb wiring across the wafer to reduce defects due to contact lithography.

Acknowledgements The South Pole Telescope is supported by the National Science Foundation through grant PLR-1248097. This work was also supported in part by the US Department of Energy under contract number DE-AC02-76SF00515. Work at Argonne National Lab is supported by UChicago Argonne, LLC, Operator of Argonne National Laboratory (Argonne). Argonne, a U.S. Department of Energy Office of Science Laboratory, is operated under Contract No. DE-AC02-06CH11357. Use of the Center for Nanoscale Materials, an Office of Science user facility, was supported by the U. S. Department of Energy, Office of Science, Office of Basic Energy Sciences, under Contract No. DE-AC02-06CH11357. Partial support is also provided by the NSF Physics Frontier Center grant PHY-1125897 to the Kavli Institute of Cosmological Physics at the University of Chicago, the Kavli Foundation and the Gordon and Betty Moore Foundation grant GBMF 947. BB is supported by the Fermi Research Alliance, LLC under Contract No. De-AC02-07CH11359 with the United States Department of Energy. NWH acknowledges additional support from NSF CAREER grant AST-0906135. JWH is supported by the NSF under Award No. AST- 1402161.The McGill authors acknowledge funding from the Natural Sciences and Engineering Research Council of Canada, Canadian Institute for Advanced Research, and Canada Research Chairs program.

References

1. A. A. Penzias and R. W. Wilson, *Astrophys. J.* **142**, 419 (1965).
2. K. N. Abazajian *et al.*, arXiv:1610.02743.
3. K. N. Abazajian *et al.*, arXiv:1706.02464.
4. B. A. Benson *et al.*, *Proc. SPIE Int. Soc. Opt. Eng.* **9153**, 91531P (2014).
5. E. M. George *et al.*, *Proc. SPIE Int. Soc. Opt. Eng.* **8452**, 84521F (2012)
6. K. D. Irwin, *Appl. Phys. Lett.* **66**, 1998 (1995).
7. A. N. Bender *et al.*, *Proc. SPIE Int. Soc. Opt. Eng.* **9153**, 91531A (2014).
8. J. Avva *et al.*, *J. Low Temp. Phys. This Special Issue.* **xx**, xxx (2017), DOI:xxxxx.
9. R. H. Duhamel, *U.S. Patent US*, 4658262 A (1987).
10. J. M. Edwards, R. O'Brient, A. T. Lee, and G.M. Rebeiz, *IEEE Trans. Antennas Propag.* **60**, 4082 (2012).
11. A. Suzuki *et al.*, *J. Low Temp. Phys.* **167**, 852 (2012).
12. R. O'Brient *et al.*, *Appl. Phys. Lett.* **102**, 63506 (2013).
13. J. Ding *et al.*, *IEEE Trans. Appl. Supercond.* **27**, 2100204 (2017).
14. J. Ding *et al.*, *J. Low Temp. Phys. This Special Issue.* **xx**, xxx (2017), DOI:xxxxx.
15. C. M. Posada *et al.*, *Supercond. Sci. Technol.* **28**, 94002 (2015).
16. C. M. Posada *et al.*, *Proc. SPIE Int. Soc. Opt. Eng.* **9914**, 991417 (2016).

17. C. L. Chang *et al.*, *IEEE Trans. Appl. Supercond.* **25**, 2500105 (2015).
18. Z. Pan *et al.*, *J. Low Temp. Phys. This Special Issue.* **xx**, xxx (2017), DOI:xxxxx.
19. F. W. Carter *et al.*, *J. Low Temp. Phys. This Special Issue.* **xx**, xxx (2017), DOI:xxxxx.
20. A. J. Anderson *et al.*, *J. Low Temp. Phys. This Special Issue.* **xx**, xxx (2017), DOI:xxxxx.
21. W. B. Everett *et al.*, *J. Low Temp. Phys. This Special Issue.* **xx**, xxx (2017), DOI:xxxxx.
22. V. G. Yefremenko *et al.*, *J. Low Temp. Phys. This Special Issue.* **xx**, xxx (2017), DOI:xxxxx.